Photo Catalytic Degradation of Azo Dyes over Mn^{2+} Doped TiO_2 Catalyst under UV/Solar Light: An Insight to the Route of Electron Transfer in the Mixed Phase of Anatase and Rutile

Lakshmipathi Naik, Gomathi Devi*[,a] Kottam, Nagaraju[a]
Shivashankar, Girish Kumar[a]

Department of Post Graduate Studies in Chemistry, Central College City Campus, Bangalore University, Bangalore-560001, India

Mn^{2+} ion was doped into the TiO_2 matrix and its photocatalytic activity was evaluated for the degradation of a mono azo dye methyl orange (MO) and a di-azo dye brilliant yellow (BY) under UV/solar light. X-ray diffraction results revealed the phase transformation from anatase to rutile due to the inclusion of Mn^{2+} ion into the TiO_2 matrix. All the doped catalysts showed a red shift in the band gap to the visible region. The degradation reaction of the dyes was found to be dependent on its structure. It was found that mono azo dye degrades faster than di azo dye under UV/solar light. The rate constant under identical conditions calculated for the degradation of MO is 2.4 times (under UV light) and 4.5 times (under solar light) higher compared to BY. Among the photocatalysts studied, Mn^{2+} (0.06 at.%)-TiO_2 showed higher activity under both UV and solar light illumination. The synergestic effect in the bicrystalline framework of anatase and rutile effectively suppresses the charge carrier recombination and enhances the photocatalytic activity. The degradation reaction was followed by UV-visible spectroscopy and the photoproducts formed were analyzed by GC-MS techniques.

Keywords Mn^{2+} doped TiO_2, synergistic effect, crystallite size, bicrystalline framework, azo dyes, photocatalytic activity under UV/solar light

Introduction

Reactive dyes are carcinogenic and are found in higher concentration in the textile industry effluents. Azo dyes constitute about 80% of the reactive dyes and these dyes are not biodegradable by aerobic treatment processes.[1] They can be decolorized by anaerobic treatment which results in the reduction of azo bonds leading to the formation of potentially carcinogenic aromatic amines.[2,3] Traditional methods such as flocculation, carbon adsorption, reverse osmosis and activated sludge process have difficulties in complete destruction of the pollutants and they simply transfer the pollutants from one phase to another. Biological methods are not recommended to treat highly toxic refractory organic pollutants. In recent years, heterogeneous photocatalysis has drawn great deal of attention to mineralize these recalcitrant organic pollutants. Among the various photocatalysts used, TiO_2 is the most preferable material due to its non-toxicity, water insolubility, stability to photocorrosion and high photoactivity.[4-10] However, high degree of recombination between photogenerated charge carriers limits the use of TiO_2. Furthermore, TiO_2 can utilize only 5% of the solar spectrum due to its wide band gap and expensive artificial UV sources should be employed for its activation. The introduction of defects through transition metal ion doping has been proved to be an effective approach to the separate charge carriers and also to shift the band gap absorption to the visible region.[11-16] Recently Arroyo *et al.*,[17] Othman *et al.*,[18] and Mohamed *et al.*,[19] have reported the formation of mixed phases when Mn^{2+} is doped into the TiO_2 matrix. Though structural characterizations were well explained, its photo catalytic activity under solar light was not explored. In this view, the present research focuses on the photocatalytic activity of Mn^{2+}-TiO_2 with bicrystalline framework of anatase and rutile under UV/solar light. An attempt has been made to provide a new physical insight related to the mechanism of charge transfer in the bicrystalline framework of anatase and rutile by taking into account, the theories of previous models. The model compound chosen is mono azo dye methyl orange (MO) and di-azo dye brilliant yellow (BY). The correlation between dye structure, pH of the reaction medium and the extent of dye adsorption, on the degrdation rate is explored in detail.

* E-mail: gomatidevi_naik@yahoo.co.in
Received September 14, 2009; revised January 21, 2010; accepted May 13, 2010.
Project supported by the UGC Major Research Project (2007-2010), Government of India.

Experimental

Materials and methods

$TiCl_4$ was obtained from Merck chemicals. MO, BY, and aqueous NH_3 were obtained from S D Fine chemicals, Bombay, India. Analytical grade MnC_2O_4•$2H_2O$ was obtained from BDH and used as received. The synonymous names for MO are p (*p*-dimethyl amino phenyl azo)-benzene sulfonate of sodium, Helanthine B, Orange III, gold orange, tropacoline D. The chemical formula is $(CH_3)_2NC_6H_4NNC_6H_4SO_3Na$ and the molecular weight is 327 and has a λ_{max} of 460—480 nm. It is an orange yellow solid soluble in water and insoluble in alcohol. The chemical formula for BY is $C_{26}H_{18}O_8N_4Na_2S_2$. The molecular weight is 312 and λ_{max} of the compound is 395 nm. The other synonymous name for BY is Direct Yellow 4.

Catalyst preparation

Anatase TiO_2 was prepared by sol-gel method through the hydrolysis of $TiCl_4$.[20] 25 mL of diluted $TiCl_4$ with 1 mL concentrated H_2SO_4 is taken in a beaker and diluted to 1000 mL. The pH of the solution was maintained at 7—8 by adding liquor ammonia. The gel obtained was allowed to settle down. The precipitate is washed free of chloride and ammonium ions. The gelatinous precipitate is filtered and oven dried at 100 ℃. The finely ground powder was then calcined at 550 ℃ for 4.5 h to get anatase polymorph of TiO_2.

A known concentration of manganese oxalate solution was added to the calculated amount of anatase TiO_2 in order to get the dopant concentration of 0.02, 0.06 and 0.1 at.% and was labelled as Mn-2, Mn-3 and Mn-4 respectively, while undoped TiO_2 was labelled as Mn-1. The mixture was ground in an agate mortar and heated in an oven at 120 ℃ for 4—5 h. The process of grinding and heating is repeated for 4 times. The sample so obtained is finally calcined at 550 ℃ for 4.5 h.

Analytical instruments

The powder X-ray diffraction (PXRD) patterns of these samples were obtained using Philips PW/1050/70/76 X-ray diffractometer which was operated at 30 kV and 20 mA with Cu Kα as a source along with a nickel filter at a scan rate of 2 (°)/min.

The average grain size was determined by the Scherrer equation: $D=k\lambda/\beta\cos\theta$, where k is the shape factor (*ca.* 0.9), λ is the X-ray wavelength (0.15418 nm), β is the full width at half maximum (FWHM) of the diffraction line and θ is the diffraction angle. The rutile fraction in the sample was calculated using the Spurr and Meyer's equation:[21] $X_R=(1+0.8I_A/I_R)^{-1}$, where X_R is the mass fraction of rutile in the prepared samples, I_A and I_R were the *X*-ray integrated intensities corresponding to the (1 0 1) diffraction plane of anatase and (1 1 0) of rutile phase respectively. The Diffuse Reflectance Spectra (DRS) were obtained using UV-visible spectrophotometer (Shimadzu-UV 3101 PC UV-VIS-NIR) with $BaSO_4$ as the reference standard. The powder samples were examined under the scanning electron microscope (Cambridge instruments) to study the surface morphology. An electron microprobe used in the EDX mode was employed to obtain qualitative information on the amount and the distribution of metal species in the sample. The specific surface area of the powders were measured by dynamic Brunauer Emmett Teller (BET) method in which N_2 gas was adsorbed at 77 K using Digisorb 2006 surface area, pore volume analyzer (Nova Quanta Chrome corporation instrument multipoint BET adsorption system).

Irradiation procedure

A typical experiment constitutes 250 mL of the 10 mg•L^{-1} dye solution in a glass reactor whose exposure surface area is 176 cm^2. The mixture is stirred in dark for 20 min to establish the adsorption equilibrium of the dye molecules on the catalyst surface. The solution is irradiated directly with the artificial UV light source of 125 W with a photon flux of 7.75 mW/cm^2 in the presence of atmospheric oxygen. The wavelength emission of the light source was in the range of 350—400 nm. The distance between the light source and the reactor is 29 cm. Experiments using solar light were carried out during the summer season between 11 am to 2 pm during which fluctuation in the solar intensity was minimal. The average intensity of the solar light was around 1200 W•cm^{-2} which is concentrated by convex lens and the reaction mixture was exposed to this concentrated solar light. To compare the efficiency of TiO_2 and Mn^{2+} doped TiO_2, all the experiments were conducted simultaneously so as to avoid errors arising due to fluctuation in solar intensity.

Analytical methods

The sample solutions were taken out from the reactor at desired time intervals and were centrifuged. The centrifugates were analyzed by UV-visible spectroscopy using Shimadzu UV-1700 Pharmaspec UV-visible spectrophotometer. These centrifugates were further extracted into non-aqueous ether medium for GC-MS analysis (GC-MS-QP 5000 Shimadzu mass spectrometer) to identify the intermediates during the course of the reaction.

Results and discussion

Catalyst characterization

PXRD patterns of Mn^{2+}-TiO_2 samples with various dopant concentrations are shown in the Figure 1. The patterns of Mn-1 and Mn-2 were indexed to only anatase phase, while Mn-3 and Mn-4 showed bicrystalline framework of anatase and rutile. Mn-3 showed higher anatase∶rutile (90∶10) ratio and Mn-4 catalyst showed higher rutile∶anatase (52∶48) ratio. These significant structural changes in the pristine TiO_2 framework due to the substitution of Mn^{2+} in Ti^{4+}

CHINESE JOURNAL OF CHEMISTRY

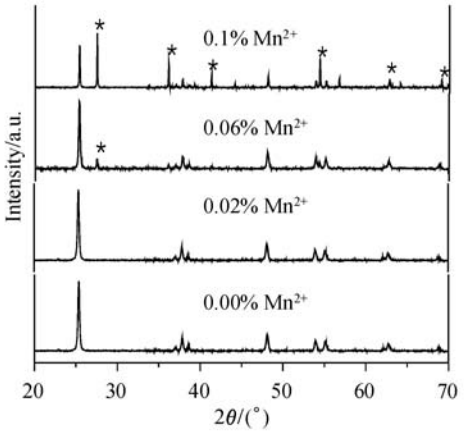

Figure 1 PXRD patterns of Mn^{2+} doped samples. The peaks with * correspond to rutile phase.

lattice sites can be explained as follows:

The large ionic size of Mn^{2+} ion (0.80 Å) compared to the host Ti^{4+} ion (0.68 Å) induces oxygen vacancies at the surface of anatase grains favoring bond rupture, solid state ionic rearrangement and structural reorganization for the nucleation of rutile phase.[22] The crystallite sizes calculated using Scherrer equation are shown in Table 1. The anatase crystallite sizes were 26.2, 23.6, 20.3 and 16.6 nm for the dopant concentration of 0.0, 0.02, 0.06 and 0.1 at.% respectively. The rutile grain size was same as that of anatase in the case of Mn-3 and Mn-4. These results suggest that Mn^{2+} doping into the TiO_2 matrix effectively inhibit the grain growth of both the phases by providing dissimilar boundaries.[23] The powders with smaller crystallites will have large number of lattice defects. The defect sites on the surface of anatase crystallite react with sites in the neighbouring anatase crystal which may or may not possess defects, favoring the formation of rutile nucleation at these sites. Further the atoms in the defect sites have higher energy than those in the main lattice and can favourably act as nucleation sites for the rutile phase formation at the surface of anatase crystallites. The higher rutile content for the sample Mn-4 is mainly due to its smaller crystallite size which is believed to contain the higher density of surface defects on the anatase crystallite. Thus the high concentration of nucleation sites for the polymorphic phase transition from anatase to rutile existing at particle-particle interface, resulting in higher fraction of rutile in Mn-4. These results suggest that phase transformation from anatase to rutile takes place in a smooth way at the intermediate concentration (0.06 at.%) and the process accelerates for higher dopant concentration (0.1 at.%). The X-ray diffraction peaks of crystal plane (101), (200) and (004) of anatase were selected to determine the lattice parameter of all the samples. The lattice parameters are obtained by using the following Eqs.

$$\text{Bragg's law: } d_{(hkl)}=\frac{\lambda}{2d\sin\theta}$$

$$\frac{1}{d^2}=\frac{h^2}{a^2}+\frac{k^2}{b^2}+\frac{l^2}{c^2}$$

where d_{hkl} is the distance between crystal planes (*hkl*), λ is the wavelength of X-ray used, *hkl* is the crystal plane indices and *a*, *b* and *c* are lattice parameters (in the anatase phase $a=b\neq c$). Since the Mn^{2+} ion has higher ionic size compared to the host Ti^{4+} ion, lattice expansions were observed for the doped samples compared to the undoped sample. The variation in the lattice parameter was reflected in the elongation of *c*-axis with increase in the Mn^{2+} concentration, confirming the substitutional incorporation of Mn^{2+} ions at Ti^{4+} lattice sites. Since only *c*-axis is changing, while *a* (=*b*) remains almost constant for the entire range of dopant concentration, it is speculated that Mn^{2+} substitutes Ti^{4+} ion preferentially on the body centered and face centered lattice sites in the anatase structure.[24]

The fundamental absorption edge in bare TiO_2 at 380 nm arises due to the electronic transition from O 2p to Ti 3d electronic levels. While in the case of doped samples, interband transition arises from the impurity level of the dopant to the band gap states of bare TiO_2. The band gap absorption shows red shift to 454 nm for Mn-3 and a large blue shift (420 nm) in absorption band is observed for higher dopant concentration (Figure 2). This provides an evidence for narrowing the band gap energy through Mn^{2+} incorporation, which endows the resulting samples with visible light harvesting ability. The band gap energies of the photocatalysts were

Table 1 Estimated anatase: rutile fraction, crystallite size (*D*), lattice parameters, unit cell volume, band gap energy (E_g) and surface area of Mn^{2+}-TiO_2 samples

Photo catalyst	A : R	*D*/nm	Lattice parameters/Å	Unit cell volume/Å^3	λ_{max}/nm	E_g/eV	Surface area/(m^2•g^{-1})
TiO_2 0.0%	100 : 0	26.42	$a=b=3.7828$ $c=9.5023$	135.97	380	3.2	18
Mn^{2+}-TiO_2 0.02%	100 : 0	23.6	$a=b=3.7832$ $c=9.5103$	136.12	426	2.9	21
Mn^{2+}-TiO_2 0.06%	90 : 10	20.3 : 20.3	$a=b=3.7824$ $c=9.5211$	136.21	454	2.7	26
Mn^{2+}-TiO_2 0.1%	52 : 48	16.6 : 16.6	$a=b=3.7800$ $c=9.5002$	135.74	420	2.9	24

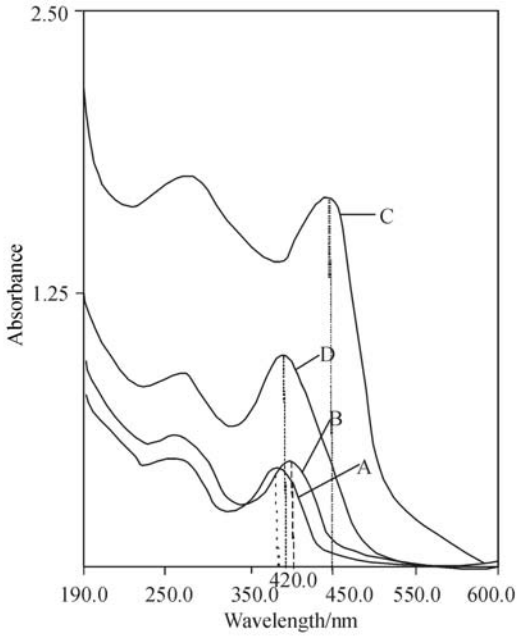

Figure 2 UV-visible absorption spectra of all the photocatalysts. (A) Mn-1, (B) Mn-2, (C) Mn-3, (D) Mn-4.

calculated by Kubleka-Munk plot of $(1-R_\infty)^2/2R_\infty$ versus wavelength. The results show that the electronic level of the dopant lies 0.5 eV below the conduction band edge of anatase (Mn-3), while in the case of Mn-2 and Mn-4, the electronic level lies *ca.* 0.3 eV below the conduction band edge of anatase. SEM images for all the samples showed almost similar morphology while EDX analysis confirmed the presence of dopant in the TiO_2 lattice (Figure 3). Surface area analysis by BET method showed higher values for doped samples compared to undoped sample, due to the introduction of additional nucleation sites by dopant and it can also be accounted to the decrease in the crystallite size of the doped samples (Table 1).

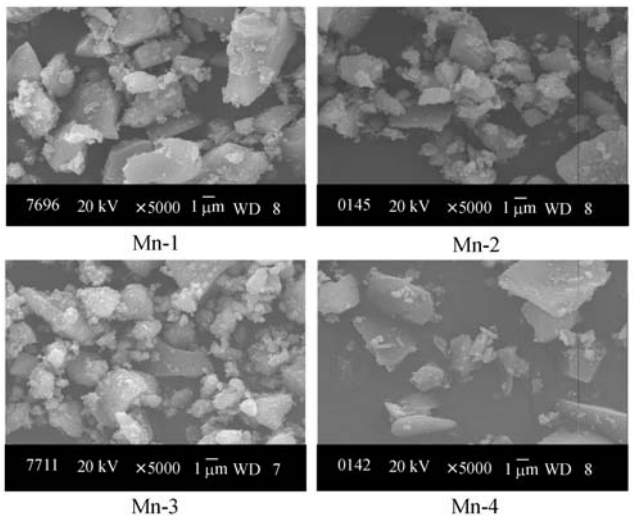

Figure 3 SEM photographs of all the photocatalysts.

Defect states induced by the dopant in the TiO_2 matrix

Manganese ions can exist either in Mn^{2+} (0.80 Å) or Mn^{3+}(0.66 Å) or Mn^{4+} (0.60 Å) oxidation states in TiO_2 matrix. The probable chemical defects created due to its inclusion in Ti^{4+} lattice sites can be predicted using Kroger and Vink notation as shown below:[25,26]

Assuming Mn^{4+} ion occupying the lattice position of Ti^{4+} in TiO_2 matrix can be represented as:

$$MnO_2 \leftrightarrow Mn_{Ti} + 2O_O \text{ (Mn in } +4 \text{ oxidation state)}$$

If the incorporation of Mn is in $+2$ or $+3$ oxidation state then it can possibly induce ionized oxygen vacancies in the TiO_2 lattice in the following way:

$$Mn_2O_3 \leftrightarrow 2Mn_{Ti}^{''} + 3O_O + V_O^{''}/2V_O^{'} \text{ (Mn is in } +3 \text{ oxidation state)}$$

$$MnO \leftrightarrow Mn_{Ti}^{''} + O_O + V_O^{''}/2V_O^{'} \text{ (Mn is in } +2 \text{ oxidation state)}$$

Charge compensation can also occur by interstitial oxygen which is less probable due to the higher ionic size of oxygen;

$$Mn_2O_3 \leftrightarrow 2Mn_{Ti}^{''} + O_i^{''} + 2O_O \text{ (Mn is in } +3 \text{ oxidation state)}$$

$$MnO \leftrightarrow Mn_{Ti}^{''} + O_i^{''} \text{ (Mn is in } +2 \text{ oxidation state)}$$

The notations V_O, $V_O^{'}$ and $V_O^{''}$ represent neutral, single and doubly ionized oxygen vacancies. Oo is oxygen occupying oxygen lattice site. Mn_{Ti} is manganese ion at titanium lattice site and the superscript bullet represents the deficiency in the charge. When Mn is in $+4$ oxidation state, its ionic radius is almost equal to Ti^{4+} ion. Hence creation of oxygen vacancies or charge imbalance in TiO_2 lattice is minimal or almost negligible. But Mn^{2+} ions has higher ionic radii compared to Ti^{4+} ion, in such a case, the charges are compensated by lattice defects such as oxygen vacancies.

Photocatalytic degradation experiments

Effect of catalyst loading

The influence of photocatalyst concentration on the degradation of the dyes was investigated in the range of 25 to 200 mg maintaining the dye concentration constant. As expected, the degradation rate was found to increase with an increase in the catalyst concentration from 25 mg to 150 mg as shown in the Figures 4 & 5. This is due to increase in the number of active sites on the catalyst surface which absorbs more number of photons, which enhances the generation of charge carriers. With increase in the catalyst loading, more number of dye molecules get preadsorbed which additionally contributes to the overall efficiency.

However, for higher catalyst loading (200 mg), the degradation efficiency decreases. This can be accounted to the following reasons:

CHINESE JOURNAL OF CHEMISTRY

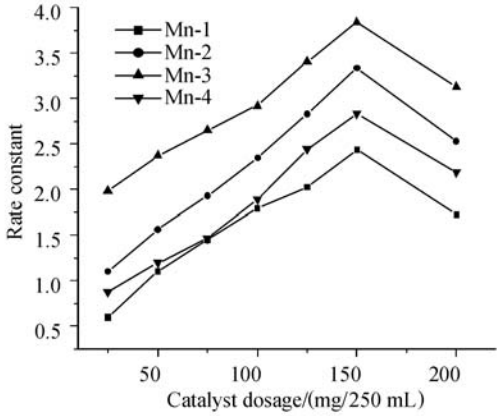

Figure 4 Effect of catalyst loading on the rate constant for the degradation of MO under UV light illumination.

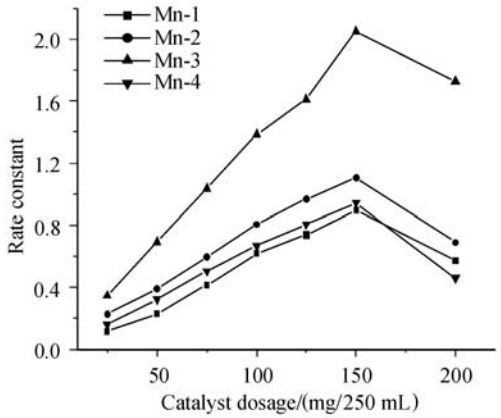

Figure 5 Effect of catalyst loading on the rate constant for the degradation of BY under UV light illumination.

Excess catalyst particles may scatter the UV light thereby reducing the generation of charge carriers.

High catalyst concentration results in shadowing effect wherein turbidity arising from the aggregation of the catalyst particles, decreases the penetration depth of light.[27]

The aggregation of TiO_2 particles covers the part of photosensitive surface thereby decreasing the number of surface active sites.

The rate constant increases with increase in catalyst dosage up to 150 mg, the effect levels off at 200 mg. Hence, an optimum catalyst loading should be maintained to ensure maximum adsorption of the dye molecules and also total absorption of photons for efficient degradation. Similar trend was also observed for doped catalysts. Therefore all the experiments were carried out at 150 mg of the photocatalyst.

Effect of initial dye concentration

The influence of dye concentration was investigated by maintaining a constant catalyst dosage at pH 5.0. With increase in the dye concentration, degradation rate decreases for the following reasons:

Non availability of the sufficient number of hydroxyl radicals.

Large number of dye molecules itself absorb photons, preventing the excitation of TiO_2 particles.[28]

Solution becomes more intense and the intensity of incident light may decrease reaching the catalyst surface.

The percentage degradation of both the dyes using all the photocatalysts at its different concentration is shown in the Table 2. The decrease in the degradation rate is more for BY compared to MO. Among the photocatalysts used, Mn-3 shows significant activity for the degradation of dyes even at higher concentration while Mn-4 showed least activity.

Table 2 Percentage degradation of dyes with different initial concentrations using various photo catalysts

Catalyst	[dye]	Degradation (MO)/%	Degradation (BY)/%
Mn-1	10	55	50
	15	43	40
	20	35	33
Mn-2	10	72	63
	15	61	50
	20	55	43
Mn-3	10	100	100
	15	76	69
	20	62	53
Mn-4	10	44	35
	15	35	35
	20	22	25

Correlation of adsorption of the dye and pH on the degradation rate

The preadsorption of the pollutant molecule (electron donor or electron acceptor) and the amount of adsorption are very important pre-requisites for efficient degradation. The aqueous dye solution along with the photocatalyst at pH 5.0 was stirred in dark for 20 min to ensure the adsorption equilibration of the dye molecules over the catalyst. The percentage of adsorption of the dye was tested by comparing its concentration before and after stirring using the formula: $(C_0-C)\times 100/C_0$, where C_0 and C are the concentration of the dye before and after stirring. From Table 3, it can be observed that the amount of dye molecules adsorbed on Mn-3 is higher. For a given dye, the magnitude of adsorption on different doped catalysts follows the order: $0.06>0.1>0.02>0.0$ at.% of Mn^{2+}. MO showed strong adsorptive tendency on the catalyst surface compared to BY. The stearic hindrance arising due to the presence of four aromatic rings may prevent the adsorption of BY dye on the catalyst surface.

The interpretation of pH effects on the photocatalytic degradation rate is a complex parameter as it involves the multiple roles such as electrostatic interaction between the semiconductor surface, solvent molecules, substrate and charged radicals formed during the degradation process. The ionization state of the catalyst

Table 3 Percentage adsorption of MO and BY dyes on the different photocatalyst surface at pH 5.0

Photo catalys	MO	BY
Mn-1	08	05
Mn-2	10	08
Mn-3	16	10
Mn-4	09	07

surface can be protonated and deprotonated under acidic and alkaline pH values as shown below:[29]

$$TiOH + OH^- \leftrightarrow TiO^- + H_2O \text{ (in alkaline medium)}$$

$$TiOH + H^+ \leftrightarrow TiOH_2^+ \text{ (in acid medium)}$$

Since the dyes can be present at different pH values in real colored effluents, the degradations of both MO and BY were carried out at three different pH values of 3.0, 5.0 and 9.0. Both the dyes are acidic in nature due to the presence of sulfonate groups. At lower pH values, catalyst surface will be positively charged and hence renders the complex formation with negatively charged sulfonate group through electrostatic force of attraction favoring stronger adsorption (Figure 6). With increase in pH, the number of positively charged active sites decreases which reduces the rate of adsorption of these dyes. At alkaline pH, both the catalyst surface and the dye molecules will be negatively charged and hence surface complexation will not be favored due to columbic repulsion between dye and catalyst surface. As a result, negligible amount of dye get adsorbed on the semiconductor particle. The rate constant for the degradation of the dyes was higher at acidic pH and low in alkaline medium which indeed correlates with the dye adsorption at different pH values on catalyst surface. However, rate constant calculated for the degradation of MO and BY at pH 5.0 was lower than the rate constant calculated at pH 3.0, despite the fact that stronger adsorption of both the dyes took place under this condition (Tables 4 & 5). The large amount of dye adsorption may prevent the photons reaching the catalyst surface and inhibits the excitation of TiO_2 particles which reduce the generation of free radicals in the solution. Therefore it is necessary to have an optimum adsorption to facilitate interfacial charge transfer process.

Photocatalytic activity

The decreases in the concentration of MO and BY using different photocatalysts under UV/solar light are shown in the Figures 7a, 7b, 8a and 8b and the corresponding rate constant values are presented in Tables 6 & 7. The photocatalytic activity increases with increase in dopant concentration up to 0.06 at.% under UV/solar light for both the dyes. The rate constant calculated for the process Mn-3/MO/UV is 3.18×10^{-2} min^{-1}, which is almost 2.3 times higher than that of Mn-1/MO/UV process. Similarly for the process Mn-3/BY/UV, it is

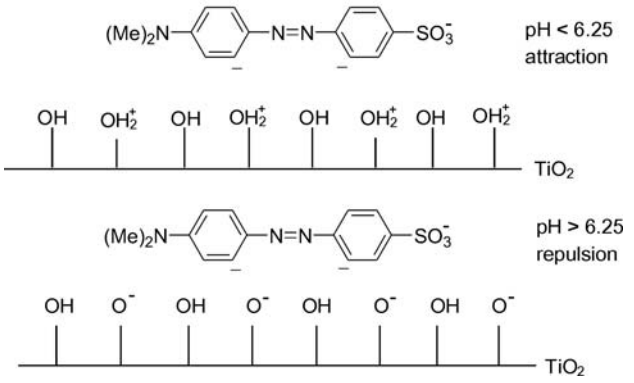

Figure 6 Surface charges above and below the iso-electric point showing the electrostatic attraction and repulsion of the MO dye molecules on the photocatalyst surface.

Table 4 Percentage adsorption and degradation, rate constant and process efficiency calculated for the degradation of MO at different pH values under UV light using Mn-3 photocatalyst[a]

Dye	pH	Adsorption/%	Degradation/%	k	Φ
	3.0	21	78	2.12	59.0
MO	5.0	16	100	3.18	75.7
	9.0	04	22	1.05	16.6

[a] k is the first order rate constant ($\times10^{-2}$ min^{-1}) calculated from the plot of $-\log(C/C_0)$ versus time. Φ is the process efficiency ($\times10^{-7}$ mg•L^{-1}•min^{-1}•W^{-1}•cm^{-2}) defined by the formula $\Phi = C/tIS$, where C is the concentration of the dye degraded in mg•L^{-1}, I is the irradiation intensity 125 W, S denotes the solution irradiated plane surface area in cm^2 and t represents the irradiation time in min.

Table 5 Percentage adsorption and degradation, rate constant and process efficiency calculated for the degradation of BY at different pH values under UV light using Mn-3 photocatalyst[a]

Dyes	pH	Adsorption/%	Degradation/%	k	Φ
	3	15	65	0.74	24.5
BY	5.0	10	100	1.30	37.8
	9	03	15	0.14	5.6

[a] k in 10^{-2} min^{-1}; Φ in 10^{-7} mg•L^{-1}•min^{-1}•W^{-1}•cm^{-2}.

1.30×10^{-2} min^{-1} which is 2.1 times higher compared to the process of Mn-1/BY/UV process. This is due to the fact that absorption intensity of fundamental edge is high for the catalyst Mn-3 which enables the catalyst to absorb more number of photons under UV light, which is also in agreement with the previous reports.[30] Further the introduction of Mn^{2+} ions into TiO_2 lattice creates mid band gap states which reduce the rate of recombination of electron and holes which additionally contributes to the overall enhancement in the process. However, the rate constant under identical conditions calculated for the degradation of MO is 2.3 times higher compared to BY. The complete degradation of MO and BY was achieved in 1 h and 2 h respectively.

CHINESE JOURNAL OF CHEMISTRY

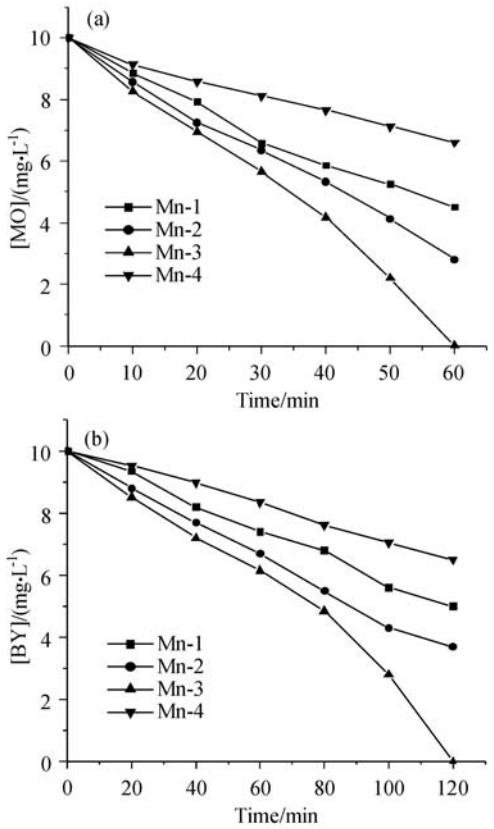

Figure 7 Plots of concentration versus time for the degradation of MO (a) and BY (b) under UV light.

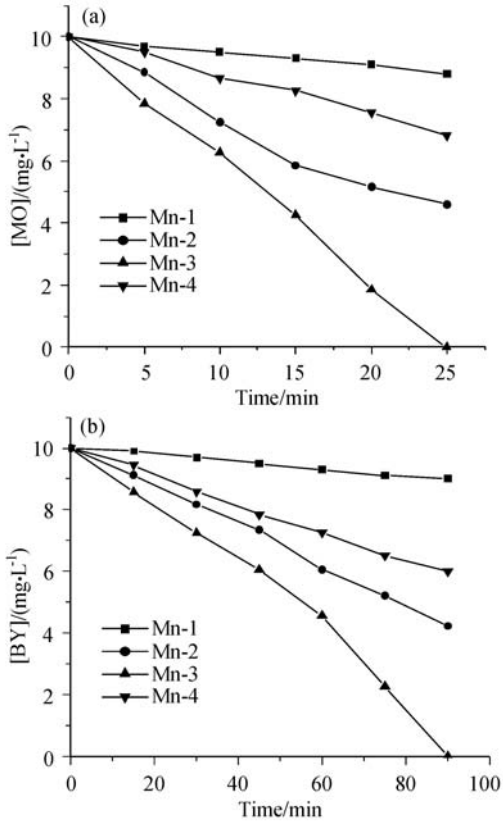

Figure 8 Plots of concentration versus time for the degradation of MO (a) and BY (b) under solar light.

Table 6 Percentage degradation, rate constant and process efficiency (Φ) for the oxidation of MO and BY under UV light[a]

Photo catalyst	Methyl orange (MO)			Brilliant yellow (BY)		
	D/%	*k*	Φ	*D*/%	*k*	Φ
Mn-1	55	1.35	41.6	50	0.62	18.9
Mn-2	72	2.14	54.5	63	0.89	23.8
Mn-3	100	3.18	75.7	100	1.30	37.8
Mn-4	44	0.61	33.3	35	0.38	13.2

[a] *D* is the percentage degradation of the dye; *k* in 10^{-2} min^{-1}; Φ in 10^{-7} mg•L^{-1}•min^{-1}•W^{-1}•cm^{-2}.

Table 7 Percentage degradation, rate constant and process efficiency (Φ) for the oxidation of MO and BY under solar light[a]

Photo catalysts	Methyl orange (MO)			Brilliant yellow (BY)		
	D/%	*k*	Φ	*D*/%	*k*	Φ
Mn-1	12	0.47	2.2	4.5	0.13	0.2
Mn-2	54	3.23	10.0	60	1.02	3.1
Mn-3	100	9.42	18.9	100	2.09	5.2
Mn-4	32	1.60	6.0	40	0.58	2.1

[a] *k* in 10^{-2} min^{-1}; Φ in 10^{-7} mg•L^{-1}•min^{-1}•W^{-1}•cm^{-2}.

Under solar light, the degradation of both the dyes was negligible with bare TiO_2. This is due to the wide-band gap which makes the catalyst inefficient to absorb visible light photons under solar light. Among the doped catalysts, Mn-3 shows higher rate constant and the degradation was achieved at a faster rate compared to UV light photocatalysis which is mainly attributed to the large red shift in the band gap which enables the catalyst to absorb more number of visible light photons. The degradation of MO and BY under solar light was completed in 25 and 90 min respectively which is faster than UV light photocatalysis. This implies that the intermediates formed under solar light were destroyed at a faster rate compared to UV light. The photocatalytic degradation of MO and BY over Mn^{2+}-TiO_2 with different dopant concentration under UV light follows the order 0.06＞0.00＞0.02＞0.1 at.%, while under solar light, the sequence is 0.06＞0.02＞0.1＞0.00 at.%. Mn-3 shows higher activity than the other photocatalysts for the degradation of both the dyes under UV/solar light which suggests that the charge carriers are effectively separated at a dopant concentration of 0.06 at.%. The magnitude of charge separation can be explained as follows: It is a well known fact that the value of space charge region potential for the efficient separation of electron-hole pairs must not be lower than 0.2 V.[31] When the dopant concentration increases from 0.02 to 0.06 at.%, the surface barrier becomes higher and the space charge region becomes narrower. The charge carriers within this region are efficiently separated by the large electric field traversing the barrier. Thus higher electric field existing within the space charge region favors the separation of photoinduced charge carriers at the expense of recombination, with a consequent in-

crease in the efficiency of the catalyst. For higher dopant concentration (0.1 at.%), surface barrier becomes higher and space charge region becomes very narrow. Thus the penetration depth of the light into the TiO_2 greatly exceeds the barrier width. The fraction of incident light generates charge carriers in the bulk of the semiconductor which do not experience any electric field, and thus the carriers can easily recombine. Hence there exists an optimum dopant concentration to create a space charge region which is substantially equal to light penetration depth.

Mechanism of charge transfer in bicrystalline framework of anatase and rutile under UV/solar light

The enhanced activity of Mn-3 under both UV/solar light was critically attributed to the bicrystalline framework of anatase and rutile which suggests the existence of synergistic effect between the mixed polymorphs. It is well known that TiO_2 with bicrystalline framework of anatase-rutile or rutile-brookite or anatase-brookite can effectively reduce the recombination of photogenerated charge carrier enhancing the photocatalytic activity.[32-56]

Under UV excitation, anatase in the mixed phase gets activated as it is a good absorber of UV light photons. The vectorial electron transfer takes place from the conduction band edge of anatase to rutile electron trapping sites. Thus rutile serves as passive electron sink hindering the recombination in anatase phase and the hole originated from the anatase transfer to the surface.[57,58] Subsequent electron transfer to impurity level of the dopant which lies *ca.* 0.5 eV below the conduction band of rutile favors effective charge separation which accelerates the interfacial charge transfer process accounting for higher efficiency of Mn-3 compared to other photocatalysts under UV light (Figure 9).

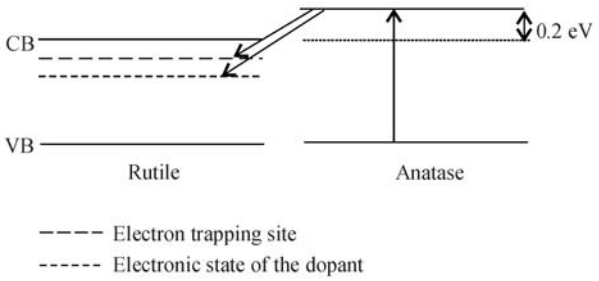

Figure 9 Charge transfer in mixed phase under UV light.

The band gap of rutile is favourable for visible light excitation as the conduction band edge of rutile lies 0.2 eV below the conduction band edge of anatase. Under visible light excitation, the photogenerated electron from conduction band of rutile vectorially transfers to electron trapping sites of anatase phase (Figure 10). This can be considered as antenna effect by rutile phase.[58,59] Subsequent transfer of electrons to lattice trapping sites of anatase/impurity level of the dopant further separates the charge carriers effectively. The lattice trapping sites of antatase has energy of 0.8 eV less than the conduction band edge of anatase.[60] Thus by competing with the recombination, the charge separation activates the catalyst and the hole originating from the rutile valence band participates in the degradation mechanism.

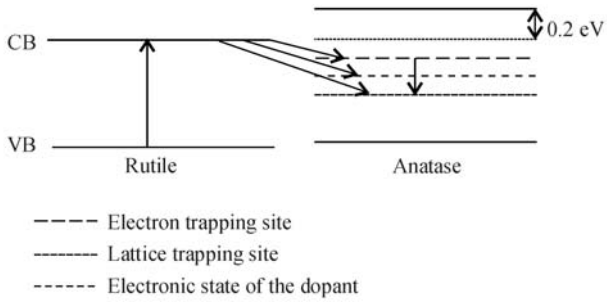

Figure 10 Charge transfer in mixed phase under solar light.

The dopant Mn^{2+} has a unique stable half filled electronic structure ($3d^5$). If Mn^{2+} is assumed to trap electrons, it gets reduced to Mn^{+} or in other case, if it traps a hole it gets oxidized to Mn^{3+}. Since both the oxidation states are highly unstable, the trapped electron will be transferred to oxygen molecule and trapped hole to surface adsorbed water or dye molecule.[61]

$$Mn^{2+} + e^{-} \rightarrow Mn^{+}$$

$$Mn^{+} + O_{2ads} \rightarrow Mn^{2+} + O_2^{-\bullet}$$

$$Mn^{2+} + h^{+} \rightarrow Mn^{3+}$$

$$Mn^{3+} + OH^{-} \rightarrow Mn^{2+} + OH^{\bullet}$$

Alternatively, the Mn^{3+} can also trap conduction band electron or Mn^{+} can trap valence band hole to retain half filled electronic structure of Mn^{2+}.

$$Mn^{+} + h^{+} \rightarrow Mn^{2+}$$

$$Mn^{3+} + e^{-} \rightarrow Mn^{2+}$$

These processes not only accelerate the interfacial charge transfer process, but it can also enhance the generation of highly reactive oxidative species like superoxide and hydroxyl radical.

In any case, the effective charge separation caused by the mixed phase structure can activate the catalyst. In order for such an interparticle electron transfer to be possible, the two polymorphs must be in close contact which mainly depends on their crystallite size. Hong *et al.*[30] prepared iodine-doped titania with mixed phases of anatase and rutile by calcining the sample at 500 ℃, which showed lower activity compared to iodine-doped anatase titania. The low activity was attributed to the large rutile crystal size compared to anatase which resulted in poor intimate contact between the mixed phases.[30] Hence it is crucial to maintain the crystallite size of both the phases which enables the mixed phase for efficient charge transfer.

CHINESE JOURNAL OF CHEMISTRY

The photocatalyst Mn-3 has anatase to rutile ratio of 90∶10 and the crystallite size being 20.3 nm for both the phases. Since the crystallite sizes of both the phases are same, it can be speculated that both the polymorphs are in intimate contact. According to Gray *et al.*[62] results, such an interfacial mixed polymorph structure would contain surplus amounts of tetrahedral Ti^{4+} sites which can act as reactive electron-trapping sites. These isolated tetrahedral Ti^{4+} sites are more active than octahedrally coordinated Ti^{4+} sites. These tetrahedral Ti^{4+}sites could serve as catalytic hot spots at anatase/rutile interface and thus avails the mixed polymorph nanocrystals into an effective photocatalytic relay for solar energy utilization.[62] Hence we believe that these tetrahedral Ti^{4+} sites contribute to the increased activity of the mixed phase relative to the pure anatase (Mn-2). The small crystallite size in Mn-3 reduces the diffusion path length for the charge carriers, from the site where they are photo produced to the site where they react. Reduction in this diffusion path length results in reduced recombination of charge carriers resulting in enhanced interfacial charge transfer process. Therefore such an intimate contact between the mixed polymorph with smaller crystallite will have a core of rutile crystallites interwoven with bound anatase crystallites, thus accelerating the transfer of electrons from rutile to neighbouring anatase sites or to the impurity level created by the dopants. However it is vital that the existence of synergistic effect between the mixed polymorphs is not universal and there exists an optimum value for both the phases to show enhanced activity. In the present case optimum value of anatase-rutile ratio is found to be 90∶10.

With the dopant concentration around 0.1 at.%, the crystallite size for both the phases is found to be 16.6 nm. In these crystallites most of the charge carriers are generated sufficiently close to the surface. As a result, the photogenerated charge carriers may quickly reach the surface resulting in faster surface recombination reaction. This is also due to the excess trapping sites in the sample and lack of driving force to separate these charge carriers. In the catalyst with smaller crystallite size, surface charge carrier recombination reaction prevails over interfacial charge transfer process. Since Mn^{2+} serves as trapping site for both electron and hole, the possibilities of trapping both the charge carriers will be high at higher dopant concentration and this trapped charge carrier may recombine through quantum tunneling.[63] Therefore there is a need for optimal dopant concentration in the TiO_2 matrix to get effective crystallite size for highest photo catalytic efficiency. Beyond the optimum dopant concentration, the rate of recombination starts dominating the reaction in accordance with the Eq. (1)

$$K_{RR} \propto \exp(-2R/a_0) \quad (1)$$

where K_{RR} is the rate of recombination, R is the distance separating the electron and hole pair, a_0 is the hydrogenic radius of the wave function for the charge carrier. As a consequence, the recombination rate increases exponentially with the dopant concentration because the average distance between the trap sites decreases with increasing number of dopant ions confined within a particle. Further it is suggested that Ti^{4+} in the TiO_2 with higher fraction of rutile is more difficult to be reduced to Ti^{3+} which suggests that trapping sites might serve as recombination centers which is in agreement with above Eq. (1).

GC-MS analysis

The GC-MS spectra recorded at 30 min shows two *m*/*z* intense peaks at 137 and 94 corresponding to the 4-hydroxy dimethyl aniline (**1**) and phenol (**2**). This suggests that the degradation proceeds through the attack of hydroxyl radicals at the active site of azo chromophore. The adsorbed sulfonate group on the catalyst surface was desorbed during the course of the reaction and might probably get eliminated as sulfuric acid. The solution after 75 min of UV irradiation showed two *m*/*z* peaks, 110 of high intensity and the other 108 of low intensity corresponding to 1,4-dihydroxybenzene (**3**) and hydroquinone **4** respectively. The demethylation of intermediate (**1**) followed by subsequent hydroxylation leads to the formation of **3**. The intermediate **3** might oxidise to **4** followed by ring opening reaction leads to the formation of maleic acid (**5**). The stepwise ring opening reactions of **5** leads to the formation of simple aliphatic acids like malonic acid (**6**), oxalic acid (**7**) and formic acid (**8**), respectively (Scheme 1).

The GC-MS spectra recorded for BY showed two *m*/*z* peaks at 110 and 212 of medium intensity and 108 of low intensity corresponding to the formation of 1,4-dihydroxybenzene (**8**), hydroxylated stillbene (**9**) and hydroquinone (**10**). This shows that the degradation of di-azo dye also proceeds through the symmetric cleavage of azo chromophore. The *m*/*z* peaks at 126 and 140 correspond to the formation of 1,2,4-trihydroxybenzene (**11**) and 2,4-dihydroxybenzyl alcohol (**12**) appearing at 60 min of UV irradiation. At 120 min of UV irradiation, mass spectra showed two *m*/*z* peaks at 78 and 94 corresponding to the formation of benzene (**13**) and phenol (**14**) (Scheme 2).

Conclusion

Mn^{2+} ion was doped into TiO_2 matrix and its photocatalytic activity was studied for the degradation of azo dyes under UV/solar light. The photocatalysts were characterized by various analytical techniques. MO showed stronger adsorption than BY on the photocatalyst surface. The inertness of two azo bonds and steric hindrance arising from the bulky aromatic rings resisted the interaction between semiconductor particles and the dye molecules which accounts for the lower degradation of BY. Among the photocatalysts used, Mn^{2+} (0.06 at.%)-TiO_2 showed higher efficiency under UV/solar light which was attributed to the synergistic effect in the

Scheme 1 Probable degradation pathway for MO

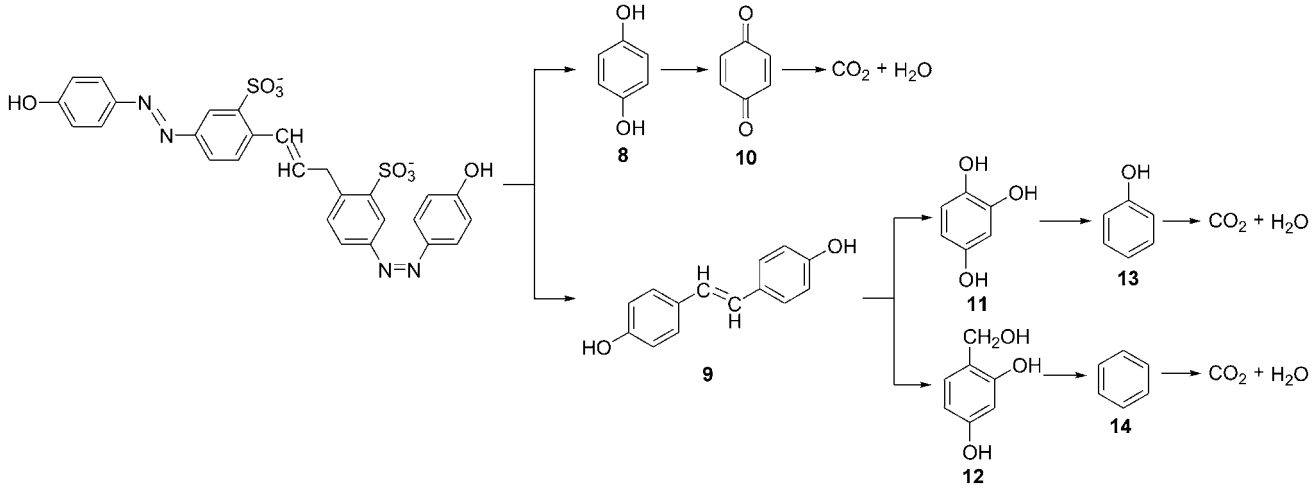

Scheme 2 Probable degradation pathway for BY

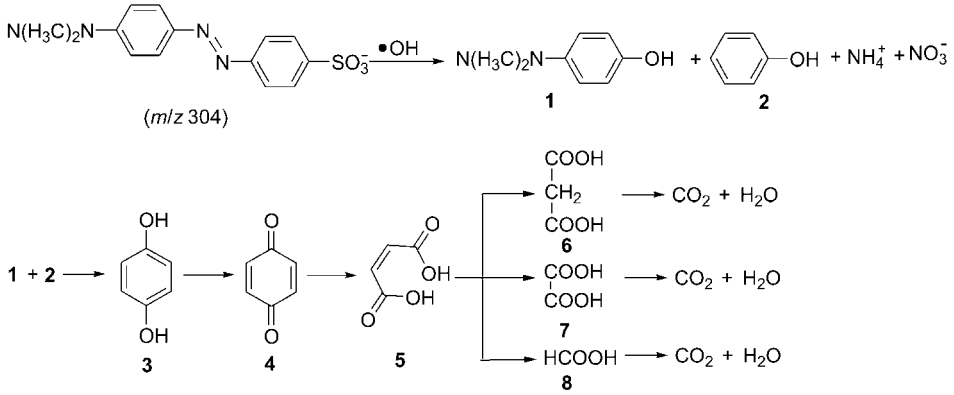

bicrystalline framework of anatase and rutile. The degradation of the dyes was followed by UV-visible and GC-MS techniques. Based on the intermediates analyzed, probable degradation mechanism has been proposed.

References

1 Pagga, U.; Drown, D. *Chemosphere* **1986**, *15*, 479.
2 Brown, B.; Hamberger, B. *Chemosphere* **1987**, *16*, 1539.
3 Chinwetkitvanich, S.; Tuntoolvest, M.; Panswad, T. *Water Res.* **2000**, *34*, 2223.
4 Jung, K. Y.; Park, S. B.; Jang, H. D. *Catal. Commun.* **2004**, *5*, 491.
5 Yu, J.; Yu, H.; Cheng, B.; Trapalis, C. *J. Mol. Catal. A*: *Chem.* **2006**, *249*, 135.
6 Yu, J.; Wang, G.; Cheng, B.; Zhou, M. *Appl. Catal. B*: *Envrion.* **2007**, *69*, 171.
7 Yu, J.; Su, Y.; Cheng, B. *Adv. Funct. Mater.* **2007**, *17*, 1984.
8 Yu, J.; Liu, S.; Yu, H. *J. Catal.* **2007**, *249*, 59.
9 Yu, J.; Zhang, L.; Cheng, B.; Su, Y. *J. Phys. Chem. C* **2007**, *111*, 10582.
10 Ooka, C.; Yoshida, H.; Takeuchi, S.; Maekawa, M.; Yamada, Z.; Hattori, T. *Catal. Commun.* **2005**, *5*, 49.
11 Choi, W.; Termin, A.; Hoffmann, M. R. *J. Phys. Chem.* **1994**, *98*, 13669.
12 Houskova, V.; Stent, V.; Bakardjieva, S.; Murafa, N.; Tyrpekl, V. *Cent. Eur. J. Chem.* **2009**, *7*, 259.
13 Hung, W. C.; Chen, Y. C.; Chu, H.; Tseng, T. K. *Appl. Surf. Sci*. **2008**, *255*, 2205.
14 Arana, J.; Diaz, O. G.; Saracho, M. M.; Rodriguez, J. M. D.; Melian, J. A. H.; Pena, J. P. *Appl. Catal. B*: *Environ.* **2002**, *36*, 113.
15 Paola, A. D.; Marci, G.; Palmisano, L.; Schiavello, M.; Uosaki, K.; Ikeda, S.; Ohtani, B. *J. Phys. Chem. B* **2002**, *106*, 637.
16 Ikeda, S.; Sugiyama, N.; Pal, B.; Marci, G.; Palmisano, L.; Noguchi, H.; Uosaki, K.; Ohtani, B. *Phys. Chem. Chem. Phys.* **2001**, *3*, 267.
17 Arroyo, R.; Corboda, G.; Padilla, J.; Lara, V. H. *Mater. Lett.* **2002**, *54*, 394.
18 Othman, I.; Mohamed, R. M.; Ibrahem, F. M. *J. Photochem. Photobiol. A*: *Chem.* **2007**, *189*, 80.
19 Mohamed, M. M.; Othman, I.; Mohamed, R. M. *J. Photochem. Photobiol. A*: *Chem.* **2007**, *191*, 153.
20 Devi, L. G.; Krishnaiah, G. M. *J. Photochem. Photobiol. A*: *Chem.* **1998**, *121*, 141.
21 Spurr, R.; Myers, W. *Anal. Chem.* **1957**, *29*, 760.
22 Chao, H. E.; Yun, Y. U.; Xingfang, H. U.; Larbot, A. *J. Eur. Ceram. Soc.* **2003**, *23*, 1457.
23 Huang, Y.; Zheng, Z.; Ai, Z.; Zhang, L.; Fan, X.; Zou, Z. *J.*

Phys. Chem. B. **2003**, *110*, 19323.
24 Burns, A.; Hayes, G.; Li, W.; Hirvonen, J.; Demaree, J. D.; Shah, S. I. *Mater. Sci. Eng. B* **2004**, *111*, 150.
25 Devi, L. G.; Murthy, B. N. *Catal. Lett.* **2008**, *125*, 320.
26 Devi, L. G.; Kumar, S. G.; Murthy, B. N.; Kottam, N. *Catal. Commun.* **2009**, *10*, 794.
27 Toor, A. P.; Verma, A.; Jotshi, C. K.; Bajpai, P. K.; Singh, V. *Dyes Pigments* **2006**, *68*, 53.
28 Nagaveni, K.; Sivalingam, G.; Hegde, M. S.; Madras, G. *Appl. Catal. B*: *Environ.* **2004**, *48*, 83.
29 Houas, A.; Lachheb, H.; Ksibi, M.; Elaioui, E.; Guillard, C.; Herrmann, J. M. *Appl. Catal. B*: *Environ.* **2001**, *107*, 4545.
30 Hong, X.; Wang, Z.; Cai, W.; Lu, F.; Zhang, J.; Yang, Y.; Ma, N.; Lin, Y. *Chem. Mater.* **2005**, *17*, 1548.
31 Park, S. B.; Jung, K. Y.; Jang, H. D. *Catal. Commun.* **2004**, *5*, 491.
32 Bessekhouad, Y.; Robert, D.; Weber, J. V. *J. Photochem. Photobiol. A*: *Chem.* **2003**, *157*, 47.
33 Zhao, L.; Han, M.; Lian, J. *Thin Solid Films* **2008**, *516*, 3394.
34 Lei, S.; Duan, W. *J. Environ. Sci.* **2008**, *20*, 1263.
35 Sun, B.; Smirniotis, P. G. *Catal. Today* **2003**, *88*, 49.
36 Lopez, T.; Gomez, R.; Sanchez, E.; Tzompantzi, F.; Vera, L. *J. Sol-gel Sci. Technol.* **2001**, *22*, 99.
37 Panpranot, J.; Kontapakdee, K.; Praserthdam, P. *J. Phys. Chem. B* **2006**, *110*, 8019.
38 Meulen, T. V. D.; Mattson, A.; Osterlund, L. *J. Catal.* **2007**, *251*, 131.
39 Bacsa, R. R.; Kiwi, J. *Appl. Catal. B*: *Environ.* **1998**, *16*, 19.
40 Jun, W.; Gang, Z.; Zhaohong, Z.; Xiangdong, Z.; Guan, Z.; Teng, M.; Yuefeng, J.; Peng, Z.; Ying, L. *Dyes Pigments* **2007**, *75*, 335.
41 Ohno, T.; Tokieda, K.; Higashida, S.; Matsumura, M. *Appl. Catal. A*: *Gen.* **2003**, *244*, 383.
42 Ohno, T.; Sarukawa, K.; Tokieda, K.; Matsumura, M. *J. Catal.* **2000**, *203*, 82.
43 Xiao, Q.; Si, Z.; Zhang, J.; Xiao, C.; Tan, X. *J. Hazard. Mater.* **2008**, *150*, 62.
44 Xiao, Q.; Si, Z.; Yu, Z.; Qiu, G. *J. Alloys Comp.* **2008**, *450*, 426.
45 Gi, L.; Chen, L.; Graham, M. E.; Gray, K. A. *J. Mol. Catal. A*: *Chem.* **2007**, *275*, 30
46 Hurum, D. C.; Agrios, A. G.; Crist, S. E.; Gray, K. A.; Rajh, T.; Thurnauer, M. C. *J. Electron Spectrosc. Relat. Phenom.* **2006**, *150*, 155.
47 Ambrus, Z.; Mogyorosi, K.; Szalai, A.; Alapi, T.; Demeter, K.; Dombi, A.; Sipos, P. *Appl. Catal. A*: *General* **2008**, *340*, 153.
48 Li, G.; Ciston, S.; Saponjic, Z. V.; Chen, L.; Dimitrijevic, N. M.; Rajh, T.; Gray, K. A. *J. Catal.* **2008**, *253*, 105.
49 Chen, L.; Graham, M. E.; Li, G.; Gray, K. A. *Thin Solid Films* **2006**, *515*, 1176.
50 Li, G.; Gray, K. A. *Chem. Phys.* **2007**, *339*, 173 and references cited therein.
51 Yan, M.; Chen, F.; Zhang, J.; Anpo, M. *J. Phys. Chem. B* **2005**, *109*, 8673.
52 Zhang, Q.; Gao, L.; Guo, J. *Appl. Catal. B*: *Environ.* **2000**, *26*, 207.
53 Xu, H.; Zhang, L. *J. Phys. Chem. C* **2009**, *113*, 1785.
54 Yu, J. C.; Zhang, L.; Yu, Y. *Chem. Mater.* **2002**, *14*, 4647.
55 Yu, J. C.; Yu, J.; Zhang, L.; Ho, W. *Chem. Commun.* **2001**, 1942.
56 Li, Y.; Li, H.; Li, T.; Li, G.; Cao, R. *Microporous Mesoporous Mater.* **2009**, *117*, 444.
57 Bickley, R. I.; Carreno, T. G.; Lees, J. S.; Palmisano, L.; Tilley, R. J. D. *J. Solid State Chem.* **1991**, *92*, 178.
58 Devi, L. G.; Kottam, N.; Kumar, S. G. *J. Phys. Chem. C* **2009**, *113*, 15593.
59 Hurum, D. C.; Agrios, A. G.; Gray, K. A.; Rajh, T.; Thurnauer, M. C. *J. Phys. Chem. B* **2003**, *107*, 4545.
60 Leytner, S.; Hupp, J. T. *Chem. Phys. Lett.* **2000**, *330*, 231.
61 Zhou, M.; Yu, J.; Cheng, B. *J. Hazard. Mater.* **2006**, *137*, 1838.
62 Li, G.; Dimitrijevic, N. M.; Chen, L.; Nichols, J. M.; Rajh, T.; Gray, K. A. *J. Am. Chem. Soc.* **2008**, *130*, 5402.
63 Zhang, Z.; Wang, C. C.; Zakaria, R.; Ying, J. Y. *J. Phys. Chem. B* **1998**, *102*, 10871.

(E0909145 Cheng, F.)

